Large-Signal Modeling and Characterization of High-Current Effects in InGaP/GaAs HBTs

Mikhail S. Shirokov, Sergey V. Cherepko, Xiaohang Du, *Member, IEEE*, James C. M. Hwang, *Fellow, IEEE*, and Douglas A. Teeter, *Member, IEEE*

***Abstract*—High-current effects in InGaP/GaAs heterojunction bipolar transistors (HBTs) were modeled and characterized. In addition to the self-heating effect, high currents were found to degrade large-signal performance mainly through Kirk and quasi-saturation effects. New formalisms in terms of base transit time and base–collector diffusion capacitance were used to modify the conventional Gummel–Poon model. This new model was verified against large-signal characteristics measured at 2 GHz. The validity of the new model for HBTs of different emitter geometry was also explored.**

***Index Terms*—Charge carrier injection, charge carrier lifetime, charge carrier processes, heterojunction bipolar transistors, microwave devices, microwave power amplifiers, semiconductor heterojunction.**

NOMENCLATURE AND TYPICAL VALUES

A. Physical Device Parameters

ε	$= 1.16 \times 10^{-12}$ F/cm. Dielectric constant of GaAs.
N_B	$= 4 \times 10^{19}$ cm^{-3}. Base doping.
x (μm)	Depth from the metallurgical base.
W_B	$= 0.08$ μm. Base thickness.
ΔW_B (μm)	$= (6)$. Extent of base push out.
ϕ_{CB}	$= \phi_{CB0} + \delta\phi_{CB}(T_J - 298)$. Collector–base built-in potential.
ϕ_{CB0}	$= 1.31$ V. ϕ_{CB} at $T_J = 298$ K.
$\delta\phi_{CB}$	$= -1.68 \times 10^{-3}$ V/K. Temperature coefficient of ϕ_{CB}.
N_C	$= 2 \times 10^{16}$ cm^{-3}. Collector doping.
W_C	$= 0.5$ μm. Collector thickness.
X_C	$= 0.5$. Area ratio of emitter mesa versus base mesa.
A_E	$= 300$ μm^2. Total emitter area.
I_B (A)	Base current.
J_B	$= I_B/A_E$. Base current density.
I_E (A)	Emitter current.
J_E	$= I_E/A_E$. Emitter current density.
I_C (A)	Collector current.
J_C	$= I_C/A_E$. Collector current density.
J_K	$= (3)$. Threshold J_C for Kirk effect.
J_Q	$= (4)$. Threshold J_C for quasi-saturation.
V_{BE} (V)	Base–emitter voltage.
V_{BC} (V)	Base–collector voltage.
V_{BCI}	$= V_{BC} + I_C R_C$. Intrinsic base–collector voltage.
V_{CE} (V)	Collector–emitter voltage.
E (V/cm)	Electric field.
PAE	Power-added efficiency.
T_C (°C)	Chuck temperature.
T_J (K)	$= 273 + T_C + \Theta I_C V_{CE}\{1 - \exp(-t/\tau_T)\}$. Junction temperature.
Θ	$= \Theta_0 + \delta\Theta(T_C - 25)$. Thermal resistance.
Θ_0	$= 280$ °C/W. Θ at $T_C = 25$ °C.
$\delta\Theta$	$= 0.57$/W. Temperature coefficient of Θ.
t (μs)	Time.
τ_T	$= 8.6$ μs. Temperature rise time.
V_T	$= kT_J/q$. Thermal voltage.
k	$= 8.62 \times 10^{-5}$ eV/K. Boltzmann constant.
q	$= 1.60 \times 10^{-19}$ C. Elementary charge.
V_{T0}	$= 26$ mV. V_T at $T_J = 298$ K.
p (cm^{-3})	Hole concentration.
n (cm^{-3})	Electron concentration.
n_C	$= (7)$. n at the junction between the extended base and remaining collector.
n_0	$= N_{SC}N_{SV}/N_C = 1.7 \times 10^{20}$ cm^{-3}. $n_C - J_C/qv_{SAT}$ with $V_{BCI} = E_G$.
N_{SC}	$= 4.7 \times 10^{17}$ cm^{-3}. Density of states in conduction band.
N_{SV}	$= 7.8 \times 10^{18}$ cm^{-3}. Density of states in valance band.
E_G	$= 1.4$ eV. Energy gap of GaAs.
D_P	$= 6.5$ cm^2/s. Hole diffusivity in extended base.
D_N	$= 78$ cm^2/s. Electron diffusivity in extended base.
μ_P	$= 250$ cm^2/Vs. Hole mobility in extended base.
μ_N	$= 3 \times 10^3$ cm^2/Vs. Electron mobility in extended base.
v_{SAT}	$= v_{SAT0} + \delta v_{SAT}(T_J - 298)$. Electron saturated velocity.
v_{SAT0}	$= 8.33 \times 10^6$ cm/s. v_{SAT} at $T_J = 298$ K.

Manuscript received July 10, 2000. This work was supported in part under the Raytheon Corporate University Relations Program and by the U.S. Air Force Research Laboratory, Sensors Directorate, Aerospace Components and Subsystems Technology Division under Contract F33615-95-1755.

M. S. Shirokov is with the Advanced Device Center, Raytheon RF Components, Andover, MA 01810 USA.

S. V. Cherepko and J. C. M. Hwang are with the Department of Electrical Engineering and Computer Science, Lehigh University, Bethlehem, PA 18015 USA.

X. Du is with RF Micro Devices, Greensboro, NC 27409 USA.

D. A. Teeter was with the Advanced Device Center, Raytheon RF Components, Andover, MA. He is now with the Boston Design Center, RF Micro Devices, Billerica, MA 01820 USA.

Publisher Item Identifier S 0018-9480(02)03017-X.

δv_{SAT} $= -1.5 \times 10^{-3}$ cm/s K. Temperature coefficient of v_{SAT}.
f (GHz) Frequency.
ω $= 2\pi f$. Angular frequency.

B. Small-Signal Model Parameters ($V_{CE} = 1.6$ *V*, $J_C = 9.3 \times 10^4$ *A/cm*^{2}, $T_C = 25°C$)

G_{BE} $= 7.72$ S. Emitter conductance.
C_{BEJ} $= 2.4$ pF. Base–emitter depletion capacitance.
C_{BED} $= 55.8$ pF. Base–emitter diffusion capacitance.
C_{CET} $= C_{BED}$. Collector–emitter transcapacitance.
G_{BC} $= 3.3 \times 10^{-5}$ S. Intrinsic collector conductance.
C_{BC} $= C_{BCJ} + C_{BCD} = 0.9$ pF. Intrinsic collector capacitance.
G_{EX} $= 6.0 \times 10^{-4}$ S. Extrinsic collector conductance.
C_{EX} $= 0.3$ pF. Extrinsic-collector capacitance.
α_F $= \alpha_0 \exp(-j\omega\tau_C)/\{1 + j\omega(\tau_B + r_E C_{BEJ})\}$. Common-base forward current gain.
α_0 $= 0.991$. DC value of α.
τ_B $= 7.3$ ps. Base transit time.
τ_C $= 0.6$ ps. Collector transit time.
r_E $= V_T/N_F I_E$. Dynamic emitter resistance.
R_{BI} $= 1.0\,\Omega$. Intrinsic base resistance.
R_B $= 0.74\,\Omega$. Extrinsic base resistance.
R_E $= 0.75\,\Omega$. Extrinsic emitter resistance.
R_C $= 2.3\,\Omega$. Extrinsic collector resistance.
L_B $= 40$ pH. Base inductance.
L_E $= 26$ pH. Emitter inductance.
L_C $= 42$ pH. Collector inductance.

C. Large-Signal Model Parameters

τ_{B0} $= 1.8$ ps. Small current base transit time.
τ_{BK} $= 12$ ps. Characteristic increase in τ_B due to Kirk effect.
J'_K $=$ (11). Semiempirical expression for J_K.
J'_{K0} $= 4.0 \times 10^4$ A/cm^2. J'_K at $T_J = 298$ K.
J_0 $= 6.6 \times 10^4$ A/cm^2. $\tau_B = \tau_{B0} + \tau_{BK}$ when $J_C = J_K + J_0$.
V_{PT} $= 2.2$ V. Collector–base punch-through voltage.
M_K $= 3.0$. Fitting parameter for J_K dependence on V_{BCI}.
τ_{BQ} $= 0.4\,\mu$s. Fitting factor for quasi-saturation.
τ_C $= \tau_{C0}(1 + \tau_{CI} J_C - \tau_{CV} V_{BCI})$. Collector transit time.
τ_{C0} $= 1.0$ ps. Low-power value of τ_C.
τ_{CI} $= 2.0 \times 10^{-5}$ cm^2/A. Current coefficient of τ_C.
τ_{CV} $= 0.36$/V. Voltage coefficient of τ_C.
I_{BF} $= (I_{CF}/\beta_F) + I_{BER}$. Base current in forward operation.
I_{CF} $= I_{SF0} \exp(V_{AF}/V_T)\{\exp(V_{BE}/N_F V_T) - 1\}$. Collector current in forward operation.
I_{SF0} $= 5.91 \times 10^3$ A. Forward collector saturation current.
V_{AF} $= 1.62$ V. Forward collector activation potential.
N_F $= N_{F0} + \delta N_F (T_J - 298)$. Forward collector ideality factor.
N_{F0} $= 1.04$. N_F at $T_J = 298$ K.
δN_F $= -6.5 \times 10^{-5}$/K. Temperature coefficient of N_F.
β_F $= \beta_{F0}/\left\{1 + (|T_J - T_{BF0}|/T_{BF})^{MBF}\right\}$. Forward current gain.
β_{F0} $= 250$. Peak value of β_F.
T_{BF0} $= 370$ K. Temperature at which β_F peaks.
T_{BF} $= 150$ K. β_F rolloff temperature.
MBF $= 4$. β_F rolloff factor.
I_{BER} $= I_{SFR0} \exp(V_{AFR}/V_T)\{\exp(V_{BE}/N_{FR} V_T) - 1\}$. Forward base–emitter current.
I_{SFR0} $= 42.9$ A. Forward base saturation current.
V_{AFR} $= 1.16$ V. Forward base activation potential.
N_{FR} $= N_{FR0} + \delta N_{FR}(T_J - 298)$. Forward base ideality factor.
N_{FR0} $= 1.52$. N_{FR} at $T_J = 298$ K.
δN_{FR} $= 3.5 \times 10^{-4}$/K. Temperature coefficient of N_{FR}.
I_{BR} $= (I_{ER}/\beta_R) + I_{BCI}$. Base current in reverse operation.
I_{ER} $= I_{SR0} \exp(V_{AR}/V_T)\{\exp(V_{BC}/N_R V_T) - 1\}$. Emitter current in reverse operation.
I_{SR0} $= 5.66 \times 10^5$ A. Reverse emitter saturation current.
V_{AR} $= 1.69$ V. Reverse emitter activation potential.
N_{R0} $= 1.12$. Reverse emitter ideality factor at 298 K.
δN_R $= -1.1 \times 10^{-4}$/K. Temperature coefficient of N_R.
β_R $= \beta_{R0} + \delta\beta_R(T_J - 298)$. Reverse current gain.
β_{R0} $= 0.55$. β_R at $T_J = 298$ K.
$\delta\beta_R$ $= -7.0 \times 10^{-4}$/K. Temperature coefficient of β_R.
I_{BCI} $= X_C I_{SRR0} \exp(V_{ARR}/V_T)\{\exp(V_{BC}/N_{RR} V_T) - 1\}$. Reverse base–collector current.
I_{SRR0} $= 12.0$ A. Reverse base saturation current.
V_{ARR} $= 0.864$ V. Reverse base activation potential.
N_{RR} $= N_{RR0} + \delta N_{RR}(T_J - 298)$. Reverse base ideality factor.
N_{RR0} $= 1.94$. N_{RR} at $T_J = 298$ K.
δN_{RR} $= -1.1 \times 10^{-4}$/K. Temperature coefficient of N_{RR}.
I_{EX} $= I_{BCI}(1 - X_C)/X_C$. Extrinsic reverse base–collector current.
R_B $= R_{B0} + \delta R_B(T_J - 298)$. Base resistance.
R_{B0} $= 0.45\,\Omega$. R_B at $T_J = 298$ K.
δR_B $= 2.3\,\text{m}\Omega$/K. Temperature coefficient of R_B.
R_E $= R_{E0} + \delta R_E(T_J - 298)$. Emitter resistance.
R_{E0} $= 0.9\,\Omega$. R_E at $T_J = 298$ K.
δR_E $= -1.2\,\text{m}\Omega$/K. Temperature coefficient of R_E.
R_C $= R_{C0} + \delta R_C(T_J - 298)$. Collector resistance.
R_{C0} $= 1.4\,\Omega$. R_C at $T_J = 298$ K.
δR_C $= 7.3\,\text{m}\Omega$/K. Temperature coefficient of R_C.
C_{BEJ} $= C_{JE}(1 - V_{BE}/\phi_{EB})^{-MJE}$. Base–emitter junction capacitance.

C_{JE} $= C_{JE0} + \delta C_{JE}(T_J - 298)$. Zero-bias base–emitter capacitance.
C_{JE0} $= 1.1$ pF. C_{JE} at $T_J = 298$ K.
δC_{JE} $= 6.87 \times 10^{-4}$ pF/K. Temperature coefficient of C_{JE}.
ϕ_{EB} $= \phi_{EB0} + \delta\phi_{EB}(T_J - 298)$. Emitter–base built-in potential.
ϕ_{EB0} $= 2.21$ V. ϕ_{EB} at $T_J = 298$ K.
$\delta\phi_{EB}$ $= -1.14 \times 10^{-3}$ V/K. Temperature coefficient of ϕ_{EB}.
MJE $= 0.45$. Emitter grading factor.
Q_{BEJ} $= \int C_{BEJ} dV_{BE}$. Base–emitter junction charge.
C_{BED} (pF) Base–emitter diffusion capacitance.
Q_{BED} $= \int C_{BED} dV_{BE}$. Base–emitter diffusion charge.
C_{BCJ} $= X_C \{C_{JC}(1 - V_{BC}/\phi_{BIC})^{-MJC} + C_{BCPT}\}$. Intrinsic base–collector junction capacitance.
C_{JC} $= C_{JC0} + \delta C_{JC}(T_J - 298)$. Zero-bias collector capacitance.
C_{JC0} $= 0.85$ pF. C_{JC} at $T_J = 298$ K.
δC_{JC} $= 1.48 \times 10^{-3}$ pF/K. Temperature coefficient of C_{JC}.
MJC $= 0.5$. Collector grading factor.
C_{BCPT} $= 0.12$ pF. Collector punch-through capacitance.
Q_{BCJ} $= \int C_{BCJ} dV_{BCI}$. Base–collector junction charge.
C_{EX} $= C_{BCJ}(1 - X_C)/X_C$. Extrinsic collector junction capacitance.
Q_{EX} $= \int C_{EX} dV_{BCI}$. Base–collector junction charge.
C_{BCD} $= (9)$. Base–collector diffusion capacitance.
Q_{BCD} $= \int C_{BCD} dV_{BCI}$. Base–collector diffusion charge.

I. Introduction

As THE trend toward lower supply voltage continues, current-induced phenomena such as the Kirk and quasi-saturation effects [1] become increasingly important for power heterojunction biploar transistors (HBTs). For example, Fig. 1 shows that, although the HBT is typically biased with a quiescent J_C of the order of 10^4 A/cm^2, under a large RF input signal, the instantaneous current can reach 10^5 A/cm^2.

The high-current effects are often mixed with high-temperature effects because, even at 1 V, a current density of 10^5 A/cm^2 can eventually increase the junction temperature by the order of 100 °C. Thus, although high-temperature effects of HBTs have been investigated extensively [2]–[11], high-current effects of HBTs have seldom been studied separately. The Kirk effect is often modeled empirically [8], [9] while the quasi-saturation effect is simply ignored. This paper attempts to analyze the high-current and high-temperature effects separately before their joint manifestation.

Through this analysis, it was found that, if the self-heating effect is under control (i.e., the HBT is thermally stable) and the operating frequency is much less than the cutoff frequency, the Kirk effect can be relatively benign. Thus, there exists wide latitude, over which significant performance improvement can be achieved by driving the HBT beyond the onset of the Kirk effect, but before the onset of the quasi-saturation effect. Therefore, the most salient feature of the present large-signal model is a newly developed forward diffusion charge model. This new charge model can account for the variation of base transit time and collector diffusion capacitance over a very wide current range. The present large-signal model eliminates the deficiencies of the standard Gummel–Poon model and accurately predicts the HBT performance under deep gain compression, as will be shown in Sections II–IV.

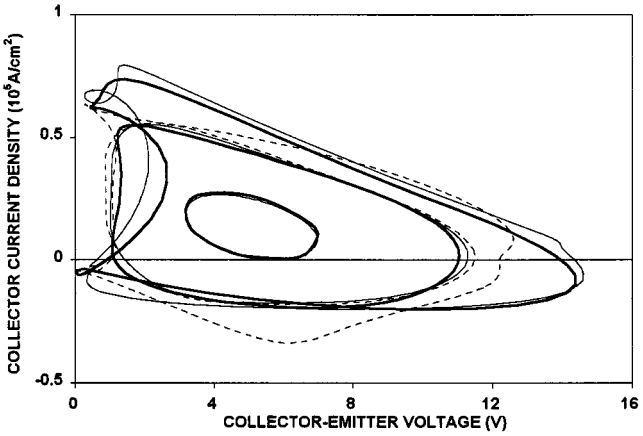

Fig. 1. **(—)** Measured dynamic load lines of a 4×75 μm^2 HBT at 2 GHz versus that (—) modeled with both high-current and high-temperature effects and (—) modeled with just the high-temperature effect. Under quiescent conditions, $V_{CE} = 5$ V and $J_B = 1.2 \times 10^2$ A/cm^2. Input and output matched for maximum PAE. $P_{\rm IN} = -5$, 5, and 15 dBm. $T_C = 25$ °C.

II. Experimental

This analysis is based on InGaP/GaAs HBT devices with one emitter finger surrounded by two base fingers and one collector finger on one side. Except in Section IV-D, the emitter finger is 4-μm wide and 75-μm long. After the HBTs are fabricated on a GaAs wafer, it is thinned to 100 μm before eutectic mounting on a copper carrier. On-wafer ground is provided by through-substrate via holes. For deembedding of parasitic pad capacitances and line delays, transmission-line test structures were fabricated together with the HBTs on the same wafer.

The HBTs were characterized under dc and RF, small- and large-signal, and CW and pulsed conditions, with $J_C = 0$ to 3×10^5 A/cm^2, $f = 2$ to 30 GHz, and $T_C = 5$ to 145 °C. Θ and T_J are extracted from the measured collector characteristics in a conventional manner [12] then reoptimized to fit all Gummel plots. A voltage supply is used to bias the base through a 33-Ω series resistor. Pulsed measurements are performed with a 3.0-μs collector voltage pulse and a 2.5-μs base voltage pulse, the leading edge of the latter trails that of the former by 0.3 μs. I_B-, I_C-, V_{BE}-, V_{BC}-, and S-parameters are sampled at 1.7 μs after the leading edge of the base voltage pulse. This time delay is a compromise between measurement accuracy and self-heating.

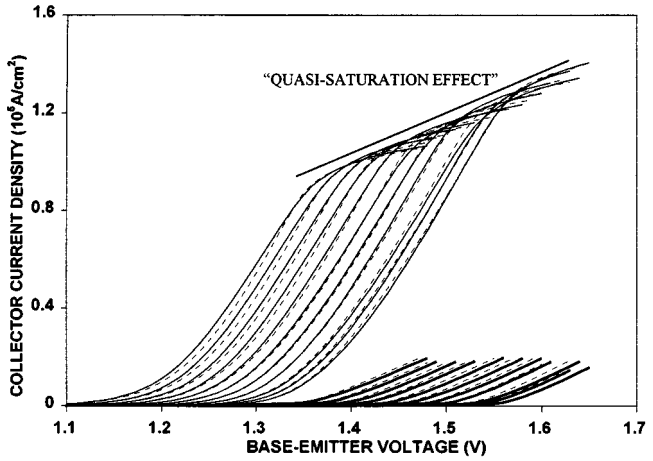

Fig. 2. Measured forward Gummel plots of (—) base and (—) collector currents versus (—) that modeled. $V_{BC} = 0$. $T_C = 5\ ^\circ\text{C}, 15\ ^\circ\text{C}, 25\ ^\circ\text{C}, 40\ ^\circ\text{C}, 55\ ^\circ\text{C}, 70\ ^\circ\text{C}, 85\ ^\circ\text{C}, 100\ ^\circ\text{C}, 115\ ^\circ\text{C}, 130\ ^\circ\text{C}$, and $145\ ^\circ\text{C}$ right to left.

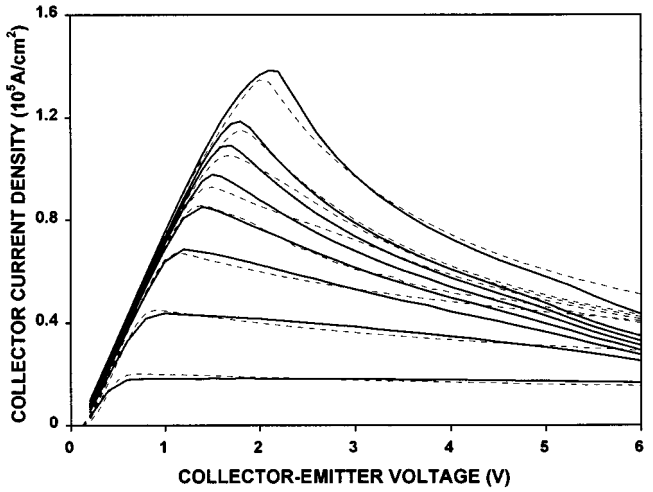

Fig. 3. (—) Measured versus (—) modeled dc collector I–V characteristics.

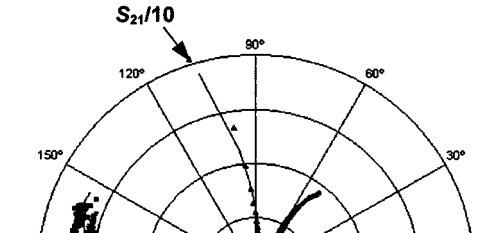

Fig. 4. (symbols) Measured versus (—) modeled S-parameters. $V_{CE} = 1.6$ V. $J_C = 9.3 \times 10^4$ A/cm^2. $T_C = 25\ ^\circ\text{C}$. $f = 1$ to 30 GHz. Arrows indicate lower frequency limits.

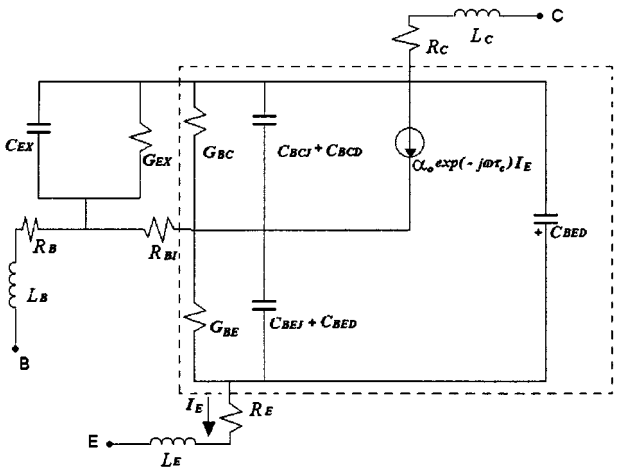

Fig. 5. Small-signal equivalent circuit model. The intrinsic HBT is encircled by a dashed line.

Assuming an exponential T_J rise over time (see Nomenclature and [13]), the amount of self-heating at 1.7 μs is reduced by approximately 80% as compared to continuous wave (CW) measurements. The pulsed measurements allow the HBTs to be characterized under very high current biases so that the Kirk and quasi-saturation effects can be better separated. Pulsed measurements also allow one to separate electrical and thermal effects. Fig. 2 shows typical forward Gummel plots. Fig. 3 shows typical collector characteristics. Fig. 4 shows typical S-parameters under a high-current and low-voltage bias.

The measured S-parameters were fitted to an equivalent —circuit model of the "T" topology (Fig. 5) in a semianalytical manner [14], [15]. In particular, τ_B and τ_C were extracted from α, after r_E was calculated from the measured dc I_E and C_{BEJ} was extracted from the so-called "cold HBT" measurement ($V_{CE} = 0$ V, $V_{BE} = 0$ V) (see [16]). The cold HBT measurement also yields C_{BCJ} and C_{EX}, after X_C is determined from the device layout. Knowing C_{BCJ}, C_{BCD} is evaluated at each bias and temperature by fitting the intrinsic Y-parameters that are obtained after deembedding the extrinsic elements from the measured S-parameters. The model parameter values for the same bias as in Fig. 4 have been included with this paper's Nomenclature.

From the small-signal equivalent-circuit models extracted at different bias points, a modified Gummel–Poon model was constructed with a new diffusion charge model (Section III). Base and collector saturation currents, ideality factors, junction capacitances, and extrinsic resistances are all made to depend on T_J. Forward and reverse saturation currents are assumed different in contrast to the standard Gummel–Poon model. Fig. 6 illustrates the large-signal model topology. Definition and typical values of the large-signal model parameters have also been included in this paper's Nomenclature.

Compared to other HBTs of comparable emitter area, the present HBTs have a relatively large R_C due to a relatively long collector finger. For the same reason, the temperature dependence of R_C is characteristic of Au instead of GaAs.

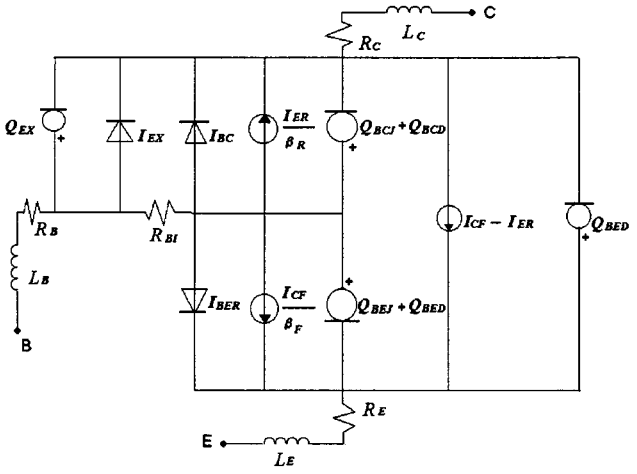

Fig. 6. Large-signal equivalent-circuit model.

The correlation between the small- and large-signal models can be found by considering the low-frequency limit of the small-signal model. From the small-signal model

$$\begin{aligned} I_C =& I_E \alpha_F(\omega) \\ =& G_{BE} V_{BE} \frac{\alpha_0 e^{-j\omega\tau_C}}{1+j\omega(\tau_B + r_{BE} C_{BEJ})} \\ \approx& \alpha_0 G_{BE} V_{BE} \left\{ 1 - j\omega(\tau_B + \tau_C + r_{BE} C_{BEJ}) \right\} \end{aligned} \quad (1)$$

$$C_{BED} = \alpha_F \tau_B G_{BE} = \frac{\partial Q_{BED}(V_{BE}, V_{BC})}{\partial V_{BE}}. \quad (2)$$

Thus, the diffusion capacitance C_{BED} and transcapacitance $C_{CET} = C_{BED}$ of the small-signal model correspond to the diffusion charge Q_{BED} of the large-signal model.

The large-signal model was installed in a commercially available harmonic-balance circuit simulator.[1] The simulated large-signal characteristics were compared with that measured. Large-signal characteristics in both frequency and time domains were measured by using an HP 71500A microwave transition analyzer. Typically, the HBT is biased with $V_{CE} = 5$ V. The base current was derived from a voltage supply through a 33-Ω series resistor, which gave a quiescent $J_C = 1.3 \times 10^4$ A/cm^2.

III. Analysis

Kirk effect occurs when $J_C \geq J_K$ so that the field at the base–collector junction vanishes. Without the retarding field, holes spill from the base into the collector, thus extending the effective base thickness. The main impact of the Kirk effect on large-signal model parameters is in terms of a longer τ_B due to the extended base thickness and a larger C_{BCD} due to the hole charge in the extended base. Following [1], the threshold collector current density for the onset of the Kirk effect may be approximated as

$$J_K = \left(1 + 2\varepsilon \frac{\phi_{CB} - V_{BCI}}{q N_C W_C^2}\right) q N_C v_{SAT}. \quad (3)$$

For the present n-p-n HBTs, $\phi_{CB} > 0$ and $V_{BCI} < 0$. Assuming $V_{BCI} = 0$, $J_K = 3.7 \times 10^4$ A/cm^2 at $T_J = 298$ K. When T_J increases due to ambient change or self-heating, J_K would decrease with increasing T_J mainly through the temperature dependence of v_{SAT}. Thus, at $T_J = 498$ K, $J_K = 2.2 \times 10^4$ A/cm^2—almost one-half of the room-temperature value.

Quasi-saturation occurs when J_C approaches another level J_Q so that most of V_{BC} drops across R_C. In this case, $\phi_{CB} \approx V_{BCI}$ and the base–collector junction is no longer reverse biased. Therefore,

$$J_Q = \frac{\phi_{CB} - V_{BC}}{R_C A_E}. \quad (4)$$

Notice that, while J_K is a threshold above which the Kirk effect becomes significant, J_Q is a practical limit so that quasi-saturation needs to be considered even when J_C is only a fraction of J_Q. In general, J_Q decreases with increasing temperature mainly through the temperature dependence of R_C. With $V_{BC} = 0$ and $T_J = 298$ K, $J_Q = 3.1 \times 10^5$ A/cm^2, which would seem too large to be relevant. However, with $T_J = 498$ K, J_Q is reduced to 1.1×10^5 A/cm^2 and becomes a real concern.

The cumulative self-heating, Kirk and quasi-saturation effects have been analyzed in detail. One-dimensional continuity equations were solved analytically for holes and electrons in the extended base under the following assumptions.

1) Quasi-neutrality is maintained in the extended base so that the hole concentration quickly drops from the order of N_B in the base to the order of N_C in the extended base then follows the same distribution as the electron concentration.
2) The electrical field is constant and low in the extended base that most of $\phi_{CB} - V_{BCI}$ drops across the remaining collector (the collector region that has not been taken over by the extended base) and holes and electrons simply diffuse through the extended base.
3) The electron diffusivity is much higher than the hole diffusivity and both satisfy the Einstein relationship [17] with the low-field mobility.
4) Electrons drift across the remaining collector at a constant v_{SAT}.

Based on these assumptions, (A3) and (A5) for electric field and electron carrier density arise (see the Appendix for a more detailed derivation). The analytical results were found in reasonable agreement with that obtained by using a commercially available two-dimensional physical device simulator.[2] Fig. 7(a) depicts the Kirk effect in terms of the distribution of electrons and holes across the extended base. In this case, n_C is independent of V_{BCI} and is a function of J_C only. Fig. 7(b) depicts the distribution of electrons and holes after the quasi-saturation effect also sets in. In this case, n_C is determined by both J_C and V_{BCI}.

Under the above assumptions and according to the derivation shown in the Appendix

$$Q_{BCD} \approx I_C \frac{(\Delta W_B)^2}{4 D_N} + q \Delta W_B n_C A_E \quad (5)$$

[1]Agilent Technologies Inc., Westlake, CA.

[2]Silvaco International, Santa Clara, CA.

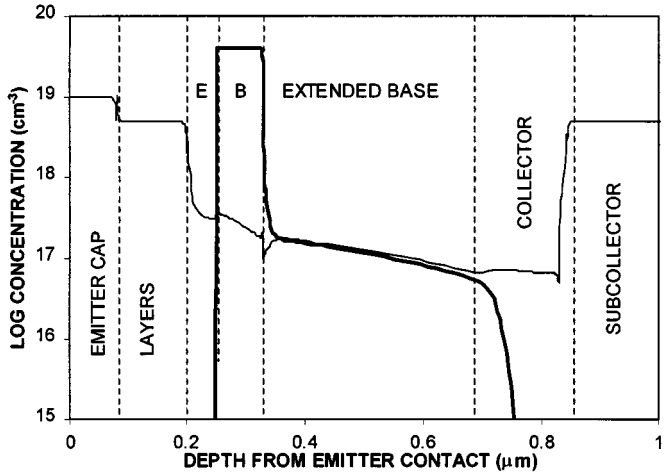

(a)

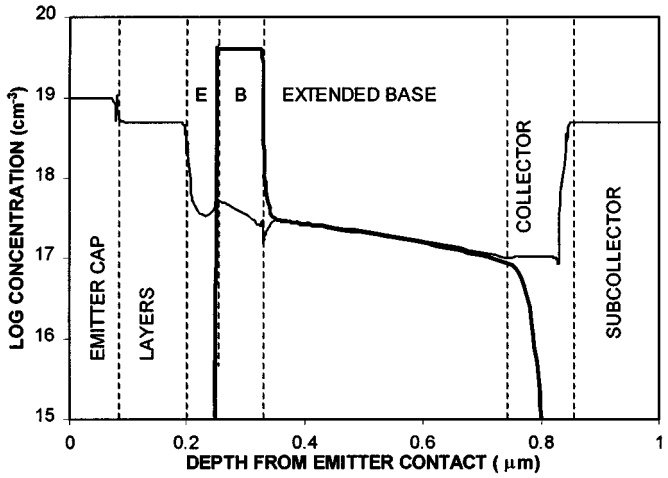

(b)

Fig. 7. Schematic illustration of (—) p and (—) n after onset of: (a) Kirk effect and (b) both Kirk and quasi-saturation effects. The self-heating effect is included in both (a) and (b). In (a), $J_C = 0.83 \times 10^5$ A/cm^2, $V_{BCI} = 0$, $\Delta W_B = 0.38\ \mu$m, $n_C = 7.1 \times 10^{16}$ cm^{-3}, and $T_J = 403$ K. In (b), $J_C = 1.3 \times 10^5$ A/cm^2, $V_{BCI} = 0.5$ V, $\Delta W_B = 0.42\ \mu$m, $n_C = 2.3 \times 10^{17}$ cm^{-3}, and $T_J = 453$ K. $Q_{BCD} = Q_{BCDF} + Q_{BCDR}$.

where according to [1]

$$\Delta W_B \approx W_C - \sqrt{\frac{2\varepsilon(\phi_{CB} - V_{BCI})}{\frac{J_C}{v_{SAT}} - qN_C}} \tag{6}$$

and by adding to the term due to J_C an additional Shockley term due to V_{BCI}

$$n_C \approx n_0 \exp\left\{\frac{qV_{BCI} - E_G}{kT_J}\right\} + \frac{J_C}{qv_{SAT}}. \tag{7}$$

Using the above equations, τ_B and C_{BCD} can be evaluated by considering the partial derivatives of Q_{BCD} with respect to J_C and V_{BCI}, respectively. The first and second terms of (5) are related to the Kirk and quasi-saturation effects, respectively. The derivative of the first term with respect to J_C can be approximated by a hyper-tangent function because ΔW_B has a sublinear dependence on J_C and is ultimately bound by W_C. On the other hand, the derivative of the second term with respect to J_C is dominated by the exponential dependence of n_C on V_{BCI}. Therefore, substituting (6) and (7) into (5) and taking corresponding derivatives of (5) yields

$$\tau_B = \tau_{B0} + \tau_{BK} \cdot F(J_C, V_{BCI}) + \tau_{BQ} e^{\frac{qV_{BCI} - E_G}{kT_J}} \tag{8}$$

$$\frac{C_{BCD}}{A_E} = \tau_{BK} \left|\frac{\partial J'_K}{\partial V_{BCI}}\right| \left\{F(J_C, V_{BCI}) - F(0, V_{BCI})\right\} + \frac{\tau_{BQ} J_C}{V_T} e^{\frac{qV_{BCI} - E_G}{kT_J}} \tag{9}$$

$$F(J_C, V_{BCI}) = 1 + \tanh\left\{\frac{J_C - J'_K}{J_0} - 1\right\} \tag{10}$$

$$J'_K = J'_{K0}\left\{1 - \frac{\delta v_{SAT}}{1\ \text{cm/s}}(T_J - 298)\right\}\left(1 + \frac{\phi_{CB} - V_{BCI}}{\phi_{CB} + V_{PT}}\right)^{M_K}. \tag{11}$$

Notice that the analytical expression of (3) has been replaced by the semiempirical expression of (11) to facilitate more accurate fitting of data.

Fig. 8 shows that (8) and (9) fit extracted τ_B and C_{BCI} reasonably well. Equations (8) and (9) were then integrated with respect to J_C and V_{BCI} to yield Q_{BCD}. Fig. 8(a) also shows that τ_C increases approximately linearly with J_C. Therefore, a treatment similar to [18] was adapted for τ_C, as listed at the beginning of this paper.

IV. Discussion

A. DC Results

Fig. 2 shows a good agreement between measured and modeled temperature-dependent forward Gummel plots. The quasi-saturation effect is obvious and is exacerbated by temperature. In comparison, the dc Kirk effect appears to be negligible. This is because the hole charge in the extended base is much smaller than that in the original base. The hole charge in the extended base can be approximated by $J_C(\Delta W_B)^2/2D_N$. With a generous estimate of $J_C = 10^5$ A/cm^2, $\Delta W_B = 0.5\ \mu$m, and $D_N = 25$ cm^2/s, $J_C(\Delta W_B)^2/2D_N \approx 5 \times 10^{-6}$ C/cm^2. By contrast, the hole charge in the original base can be approximated by $qN_BW_B = 6 \times 10^{-5}$ C/cm^2.

By properly accounting for the temperature dependence of thermal resistance, saturation currents, ideality factors, and terminal resistances, Fig. 3 shows that the modeled and measured collector characteristics are also in good agreement up to 3×10^5 W/cm^2 dissipated power under which severe self-heating takes place. Notice that, although power dissipation at the quiescent point is approximately 1×10^5 W/cm^2, under a large RF drive, dissipated power can increase to 3×10^5 W/cm^2 due to the self-biasing effect. In this case, both high-temperature and high-current effects need to be modeled accurately.

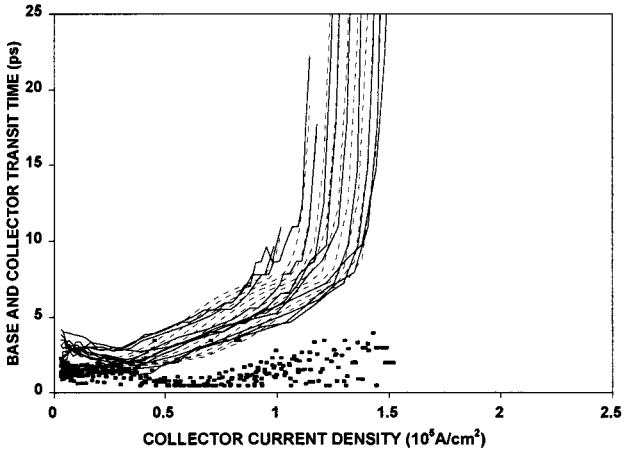

(a)

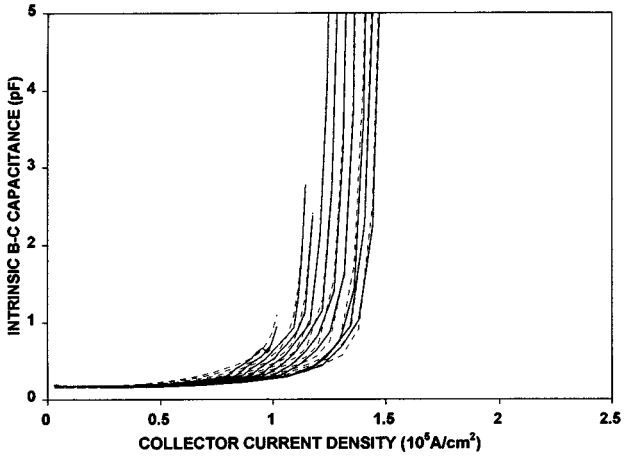

(b)

Fig. 8. (a) (—) Extracted versus (—) modeled base transit time as well as (■) extracted collector transit time. (b) (—) Extracted versus (—) modeled intrinsic base–collector capacitance. $V_{BC} = -1$ V. $T_C = 5\ ^\circ\text{C}, 15\ ^\circ\text{C}, 25\ ^\circ\text{C}, 40\ ^\circ\text{C}, 55\ ^\circ\text{C}, \ldots, 145\ ^\circ\text{C}$ right to left.

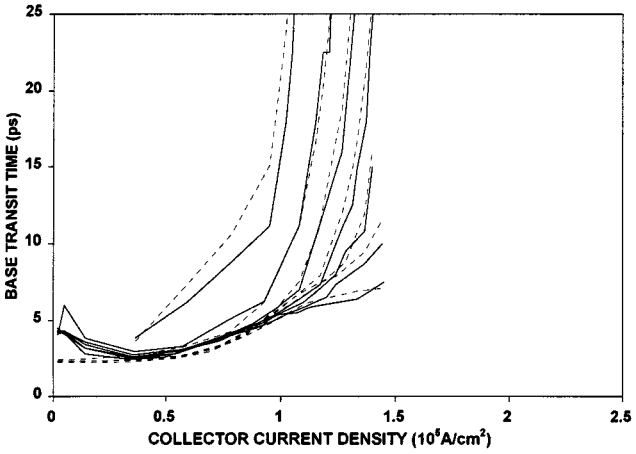

(a)

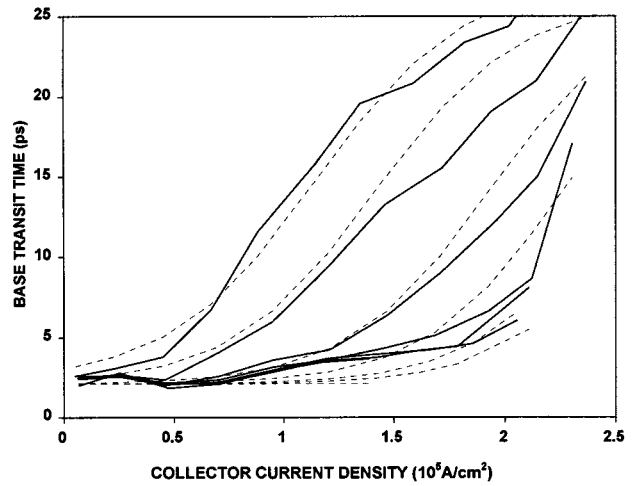

(b)

Fig. 9. (—) Extracted base transit time at different intrinsic base–collector voltages under: (a) CW and (b) pulsed bias conditions versus that (—) fitted. $T_C = 25\ ^\circ\text{C}$. (a) $V_{BCI} = 0.65, 0.7, 0.75, 0.8, 0.85, 0.9$, and 1.0 V and (b) -0.5, $-0.25, 0, 0.25, 0.55, 0.75$, and 1.0 V right to left.

B. Small-Signal Results

Depending on the current density, different interplays between the self-heating, Kirk, and quasi-saturation effects are manifested. For example, for J_C between approximately 0.4 and 1.2×10^5 A/cm^2, the Kirk effect dominates so that τ_B and C_{BCI} increase approximately linearly with J_C. However, the temperature and quasi-saturation effects cannot be entirely ignored even within this current range. The effect of temperature on J_K was discussed in Section III and is reflected in Fig. 8. To separate out the effect of quasi-saturation, Fig. 9(a) replots τ_B at $T_C = 25$°C under different V_{BCI} values. It can be seen that so long as $V_{BCI} < 0.65$, τ_B increases approximately linearly with J_C under CW conditions.

For $J_C \geq 1.2 \times 10^5$ A/cm^2, the quasi-saturation effect dominates under CW conditions so that τ_B and C_{BCI} increase exponentially with J_C, as predicted by (8), given the linear relationship between J_C and V_{BCI}. On the other hand, under pulsed test conditions, self-heating, hence, quasi-saturation, is significantly reduced, and the region where the Kirk effect dominates can be further extended. Fig. 9(b) plots τ_B extracted from pulsed S-parameters under different V_{BCI} values. It can be seen that as long as $V_{BCI} < 0$, τ_B would increase approximately linearly even for $J_C \approx 2 \times 10^5$ A/cm^2.

C. Large-Signal Results

Fig. 10 shows the power performance at 2 GHz with the input and output matched for maximum PAE. Up to seven harmonics were included in both measurement and simulation. In each case, the measured performance was compared with that modeled with the cumulative self-heating, Kirk, and quasi-saturation effects, or with just the self-heating effect.

In general, both models are in good agreement with the measured fundamental output power and gain. However, without the relatively abrupt quasi-saturation effect, the model with just self-heating underestimates even harmonics, but overestimates odd harmonics. In addition, the model with just self-heating underestimates the dc current level hence underestimates the junction temperature, but overestimates the efficiency. In comparison, the model with the cumulative self-heating, Kirk, and quasi-saturation effects are in agreement with all aspects of power performance, even under deep gain compression.

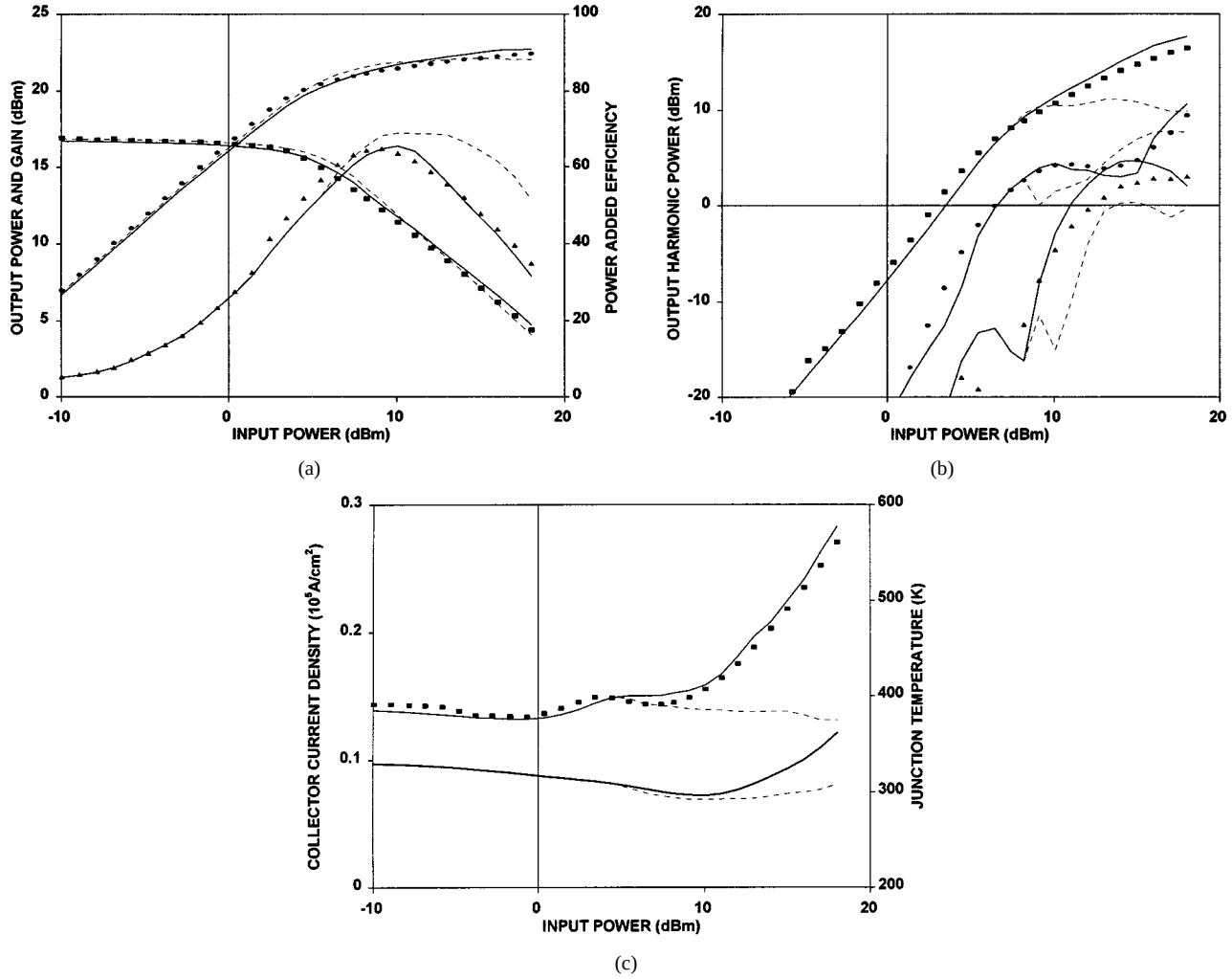

Fig. 10. (a) (•) Fundamental output power, (■) gain, and (▲) PAE. (b) (■) second, (•) third, and (▲) fourth harmonic output power. (c) (■) collector current density and **(—)** junction temperature measured at 2 GHz on an HBT that is matched for maximum PAE. (—) Modeled with both high-current and high-temperature effects. (—) Modeled with the high-temperature effect only. Under quiescent conditions, $V_{CE} = 5$ V. $J_B = 1.2 \times 10^2$ A/cm^2.

The deficiency of the self-heating only model is probably caused by neglecting the displacement current associated with C_{BCD}, thereby underestimating harmonic powers and currents associated with the displacement current when the HBT is driven into compression. This is consistent with the dynamic load lines measured under the same conditions, as shown in Fig. 1.

Measured and modeled power performance under other bias, match and drive conditions are in similar agreement. The present large-signal model is based on smooth functions such as hyper tangent and exponential functions, and is specifically designed for robust harmonic-balance simulation of power HBTs. Typically, convergence is reached within the same time frame as that of the standard (without any modification for self-heating or quasi-saturation effect) Gummel–Poon model.

According to (8), increase in τ_B by the Kirk effect alone (before quasi-saturation) is rather moderate. For example, at $T_C = 25$°C, τ_B increases from 2 to 5 ps when J_C increases from 0 to 10^5 A/cm^2. Such an increase in τ_B was found to have relatively mild impact on large-signal performance at 2 GHz, but may be more critical at higher frequencies.

The simulation of Fig. 10 has been repeated with or without the Kirk effect ($\tau_{BK} = 12$ ps or 0), but always with self-heating and quasi-saturation effects. It was found that, under light compression, the Kirk effect reduced power gain by approximately 0.5 dB and PAE by approximately 3%. The Kirk effect also reduced clipping in the time-domain waveforms, hence, increased even harmonics. For example, the second harmonic was reduced by approximately 2 dB under the same input power. This is because without the Kirk effect, the HBT has a higher gain and compresses at a lower input power level.

We also performed the simulations at $V_{CE} = 3$ V and found that when output match was compromised for peak PAE and P_{OUT}, the Kirk effect was still shunt by the quasi-saturation under heavy compression. Similar simulations were repeated under the same bias conditions, but with the input and output matched for the maximum output power at 10 GHz. In this case, reduction of power gain of ∼2.5 dB and PAE of ∼10% was found due to the Kirk effect under slight compression. This confirms that the Kirk effect will have a more severe impact when the frequency approaches a significant fraction of the cutoff frequency of the HBT.

TABLE I
EFFECT OF EMITTER GEOMETRY

Emitter Width (μm)	Emitter Length (μm)	Collector Resistance R_{C0} (Ω)	Thermal Resistance Θ_0(°C/W)
3	100	0.9	200
4	75	1.4	280
6	50	1.8	350

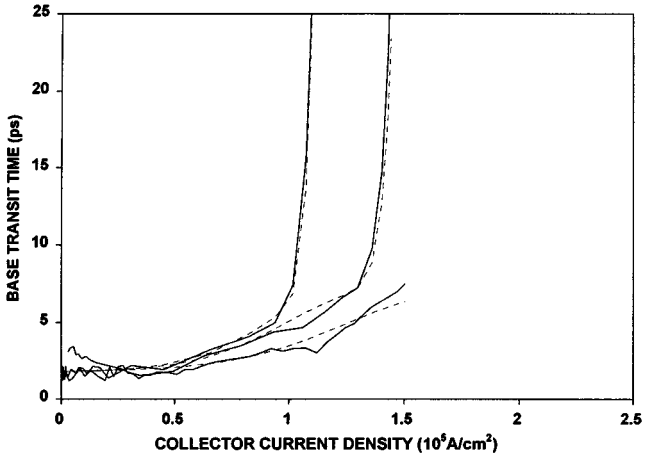

Fig. 11. (—) Extracted versus (—) modeled base transit time for an emitter of 3×100, 4×75, and 6×50 μm^2 right to left. $V_{BC} = -1$ V. $T_C = 25$°C.

D. Effect of Emitter Geometry

Since the emitter geometry can potentially affect other high-current effects such as the emitter crowding effect [1], two additional types of HBTs with a narrower or wider emitter, but the same emitter area were characterized. The results were then compared with the first type of HBTs. As shown in Table I, the main effect of emitter geometry was for thermal and collector resistances to increase with emitter width, as one would expect by inspecting the layout of the devices. Once the proper values of Θ and R_C are used in the model, the model predicts the correct characteristics such as τ_B for all three types of HBTs (Fig. 11). Therefore, the emitter crowding effect appears to be negligible in the present HBTs, probably due to their relatively high gain.

E. Comparison With Literature

The Kirk effect has been extensively studied in Si bipolar junction transistors (BJTs) [19]. Base push-out was deemed as a possible cause for the observed bending in dc I–V characteristics at high currents. Recently, a physics-based model was reported for a high-speed Si BJT in which τ_B was considered as a function of J_C, V_{CE}, and T_J [20] . At high V_{CE}, the model predicted a gradual increase of τ_B after the onset of the Kirk effect, which was followed by saturation of τ_B for $J_C \geq 3.5 \times 10^5$ A/cm^2. Such a behavior is very similar to that predicted by the hyper tangent term of (8). At low V_{CE}, [20] reported a steep increase in τ_B, but did not dwell upon the reason. The similarity between their results and the present observation suggests self-heating, as well as quasi-saturation effects are responsible for such a steep increase of τ_B.

By comparison, none of the large-signal HBT models known to us considers the base–collector diffusion charge under quasi-saturation. The quasi-saturation effect has not been considered in HBTs perhaps because HBTs are not expected to sustain as high a static current density as the BJTs due to the more severe self-heating effect in HBTs. However, this paper shows that high current density can be reached momentarily under large RF swings, whereas the more severe self-heating effect can bring about the quasi-saturation effect at a lower current density.

Recently, an empirical model was reported for the Kirk effect in HBTs in which τ_B was modeled as an exponential function of J_C [9]. The studies in this work indicate that more accurate modeling of τ_B occurs by separating contributions from the Kirk effect and the quasi-saturation effect. As explained in Sections III and IV-B, the contribution to τ_B from the Kirk effect is gradual and eventually saturates with increasing J_C. At very high current density, an exponential dependence of τ_B on J_C is observed, but it is due to the quasi-saturation effect, not the Kirk effect. Although the empirical model of [9] apparently works in the medium current range, when extended to higher currents, it may erroneously regard quasi-saturation as an extension of Kirk effect.

V. CONCLUSION

Accurate prediction of HBT large-signal characteristics under high currents is important because, as the trend for lower supply voltage continues, higher peak currents are required for RF power generation. It was found that, in addition to cause self heating, high currents can cause Kirk and quasi-saturation effects that are critical for large-signal characteristics of InGaP/GaAs HBTs, especially when these HBTs are driven into heavy compression to maximize their power output or efficiency. Other high-current effects, such as the emitter crowding effect, appear not as important for the present devices.

APPENDIX
DERIVATION OF (5)

The total electron charge in the extended base can be obtained by integrating the electron distribution there after the onset of the Kirk effect. Electron distribution can be obtained by solving the continuity equation

$$D_N \frac{\partial n(x)}{\partial x} + \mu_N E(x) n(x) = \frac{-J_C}{q} \tag{A1}$$

assuming the collector current is mostly carried by electrons due to their higher diffusivity than that of holes. On the other hand, the electrical field can be found by solving the continuity equation for holes

$$-D_P \frac{\partial p(x)}{\partial x} + \mu_P E(x) p(x) \approx 0. \tag{A2}$$

Thus,

$$E(x) \approx \frac{D_P}{\mu_P} \frac{1}{p(x)} \frac{\partial p(x)}{\partial x} = \frac{D_N}{\mu_N} \frac{1}{n(x)} \frac{\partial n(x)}{\partial x} \tag{A3}$$

according to the quasi-neutral assumption $n(x) \approx p(x)$ (neglecting N_C) and the Einstein relationship. Substituting (A3) into (A1)

$$\frac{\partial n(x)}{\partial x} = \frac{-J_C}{2qD_N}. \tag{A4}$$

Integrating (A4) with respect to x with the boundary condition $n(\Delta W_B) = n_C$, we have

$$n(x) = n_C + \frac{J_C}{2qD_N} \cdot (\Delta W_B - x). \tag{A5}$$

Finally, (5) can be obtained by integrating (A5) once more with respect to x and multiplying the result with qA_E.

ACKNOWLEDGMENT

The authors are grateful for the assistance of S. Halder, Nanyang Technological University, Singapore, and Dr. G. I. Ng, Nanyang Technological University, Singapore, in pulsed and a portion of load–pull measurements. The authors would also like to acknowledge the helpful discussion with Dr. W. Liu, Texas Instruments Incorporated, Dallas, TX.

REFERENCES

[1] W. Liu, *Handbook of III–V Heterojunction Bipolar Transistors*. New York: Wiley, 1998, pp. 233–331.
[2] P. C. Grossman and J. Choma, "Large-signal modeling of HBT's including self-heating and transit time effects," *IEEE Trans. Microwave Theory Tech.*, vol. 40, pp. 449–463, May 1992.
[3] K. Fricke, H. Hartnagel, W.-Y. Lee, and J. Wurfl, "AlGaAs/GaAs HBT for high-temperature applications," *IEEE Trans. Electron Devices*, vol. 39, pp. 1977–1980, Sept. 1992.
[4] D. S. Whitefield, C. J. Wei, and J. C. M. Hwang, "Elevated temperature microwave characteristics of HBT's," in *IEEE GaAs IC Symp. Dig.*, 1992, pp. 267–270.
[5] P. Baureis and D. Seitzer, "Parameter extraction for HBT's temperature dependent large-signal equivalent circuit model," in *IEEE GaAs IC Symp. Dig.*, 1993, pp. 263–266.
[6] J. P. Balbe *et al.*, "Theory and experiment of the temperature dependence of AlGaAs/GaAs HBT's characteristics for power amplifier applications," *Solid State Electron.*, vol. 38, no. 2, pp. 279–286, 1995.
[7] K. Lu, P. Perry, and T. Brazil, "A new large-signal AlGaAs/GaAs HBT model including self-heating effects, with corresponding parameter extraction procedure," *IEEE Trans. Microwave Theory Tech.*, vol. 43, pp. 1433–1445, July 1995.
[8] C. J. Wei, J. C. M. Hwang, W.-J. Ho, and J. A. Higgins, "Large-signal modeling of self-heating, collector transit-time, and RF-breakdown effects in power HBT's," *IEEE Trans. Microwave Theory Tech.*, vol. 44, pp. 2641–2646, July 1996.
[9] L. Camnitz, S. Kofol, T. Low, and S. Bahl, "An accurate, large signal, high frequency model for GaAs HBT's," in *IEEE GaAs IC Symp. Dig.*, 1996, pp. 303–306.
[10] Q. Zhang, H. Hu, J. Sitch, R. Surridge, and J. Xu, "A new large-signal HBT model," *IEEE Trans. Microwave Theory Tech.*, vol. 44, pp. 2001–2009, Nov. 1996.
[11] D. Ahmari *et al.*, "Temperature dependence of InGaP/GaAs HBT dc and small-signal behavior," *IEEE Trans. Electron Device*, vol. 46, pp. 634–640, Apr. 1999.
[12] D. E. Dawson, A. K. Gupta, and M. L. Sahib, "CW measurement of HBT thermal resistance," *IEEE Trans. Electron Devices*, vol. 39, pp. 2235–2240, Oct. 1992.
[13] D. S. Whitefield, C. J. Wei, and J. C. M. Hwang, "Temperature-dependent large-signal model of HBT's," in *IEEE GaAs IC Symp. Dig.*, 1992, pp. 221–224.
[14] C. J. Wei and J. C. M. Hwang, "Direct extraction of equivalent circuit parameters for heterojunction bipolar transistors," *IEEE Trans. Microwave Theory Tech.*, vol. 43, pp. 2035–2040, Sept. 1995.
[15] B. Li, S. Prasad, L.-W. Yang, and S. C. Wang, "A semianalytical parameter-extraction procedure for HBT equivalent circuit," *IEEE Trans. Microwave Theory Tech.*, vol. 46, pp. 1427–1435, Oct. 1998.
[16] D. R. Pehlke and D. Pavlidis, "Direct calculation of the HBT equivalent circuit from measured S-parameters," in *IEEE MTT-S Int. Microwave Symp. Dig.*, vol. 2, 1992, pp. 735–738.
[17] S. M. Sze, *Physics of Semiconductor Devices*, 2nd ed. New York: Wiley, 1981, p. 30.
[18] C. J. Wei, H.-C. Chung, and J. C. M. Hwang, "A compact large-signal power HBT model which includes high-current effects," presented at the Sarnoff Symp., 1997.
[19] R. J. Whitter and D. A. Tremere, "Current gain and cutoff frequency falloff at high currents," *IEEE Trans. Electron Devices*, vol. ED-16, pp. 39–57, Jan. 1969.
[20] M. Schroeter and T.-Y. Lee, "Physics-based minority charge and transit time modeling for bipolar transistors," *IEEE Trans. Electron Devices*, vol. 46, pp. 288–300, Feb. 1999.

Mikhail S. Shirokov was born in Moscow, Russia, in 1973. He received the Diploma degree in microelectronics from the Moscow Engineering Physics Institute, Moscow, Russia, in 1995, and the M.S. and Ph.D. degrees from Lehigh University, Bethlehem, PA, in 1998 and 2000, respectively.

He is currently a Senior Electrical Engineer with Raytheon RF Components, Andover, MA. His research interests include modeling and characterization of microwave devices and circuits and monolithic microwave integrated circuit (MMIC) design for wireless communication applications.

Sergey V. Cherepko received the M.S. degree in electrical engineering from the Moscow Engineering Physics Institute, Moscow, Russia, in 1995.

He was primarily interested in ionizing radiation and hot carrier effects in Si MOS and BJTs. Since 1999, he has been a Research Assistant with the Electrical Engineering and Computer Science Department, Lehigh University, Bethlehem, PA. His current research activities include RF and dc modeling and characterization of GaAs, InGaP/GaAs, and InP HBTs.

Xiaohang Du (M'99) received the B.S. degree in electrical engineering from Tsinghua University, Beijing, China, in 1993, and the M.S. degree in electrical engineering from Lehigh University, Bethlehem, PA, in 1998.

He is currently a Design Engineer with RF Micro Devices, Greensboro, NC, where he concentrates on power-amplifier design for wireless applications.

James C. M. Hwang (M'81–SM'82–F'94) the B.S. degree in physics from National Taiwan University, Taiwan, R.O.C., in 1970, and the M.S. and Ph.D. degrees in materials science and engineering from Cornell University, Ithaca, NY, in 1973 and 1976, respectively.

He possesses 12 years of industrial experience with IBM, AT&T, GE, and GAIN. In 1988, he joined Lehigh University, Bethlehem, PA, where he is currently a Professor of electrical engineering and Director of the Compound Semiconductor Technology Laboratory. He also currently holds a part-time appointment as a Professor at the Nanyang Technological University, Singapore. He has been a consultant for the U.S. Government and many electronic companies in the area of RF/microwave devices and integrated circuits. He co-founded GAIN and QED, and saw the former go bankrupt while the latter become a public company. He has authored or co-authored approximately 150 technical papers. He holds four U.S. patents.

Douglas A. Teeter (S'85–M'87) received the B.S.E.E. degree from the Virginia Polytechnic Institute and State University, Blacksburg, in 1987, and the M.S., and Ph.D. degrees in electrical engineering from The University of Michigan at Ann Arbor, in 1988 and 1992, respectively.

From 1992 to 2000, he was with the Raytheon Advanced Device Center Research Laboratories, Andover, MA, and Research Divisions, Lexington, MA, where he was responsible for development of HBT, pseudomorphic high electron-mobility transistor (pHEMT), and metamorphic high electron-mobility transistor (MHEMT) devices, models, and circuits. From 1995 to 1998, he led Raytheon's Model Development Group, and from 1998 to 2000, he led the Advanced Circuit Development Group. In 2000, he joined RF Micro Devices, Greensboro, NC, where he currently designs power amplifiers and develops new technology for next-generation handsets. His research interests include compound semiconductor devices, circuit design, and device modeling.